PERGAMON

Journal of the Mechanics and Physics of Solids
47 (1999) 1131–1155

JOURNAL OF THE
MECHANICS AND
PHYSICS OF SOLIDS

An axisymmetric model of pore-grain boundary separation

H. H. Yu, Z. Suo*

Mechanical and Aerospace Engineering Department and Princeton Materials Institute, Princeton University, Princeton, NJ 08544, U.S.A.

Received 24 June 1998; accepted 1 September 1998

Abstract

In the final stage of ceramic sintering, pores can either move with, or separate from, grain boundaries. The outcome is critical to the resulting ceramics. This paper studies an axisymmetric model of a single pore on a moving grain boundary. Two rate processes, grain boundary migration and surface diffusion, are concomitant. Surfaces move to reduce the total surface and grain boundary energy. A finite element method is formulated to simulate the transient separation process. Using an independent method, we also obtain steady state solutions of the pore moving with the grain boundary. The steady state problem has multiple solutions with a surprisingly rich mathematical structure. Finite element simulations show that some steady state solutions are stable, and others unstable. We find that the pore–grain boundary separation condition is insensitive to the dihedral angle.

Keywords: Surface diffusion; Grain boundary migration; Surface energy; Ceramic sintering; Finite elements

1. Introduction

In the final stage of ceramic sintering, pores and grains co-evolve to reduce the total surface and grain boundary energy (Coble, 1960). Individual pores are isolated, sitting on grain boundaries, three-grain junctions, and four-grain junctions. Pores shrink as atoms elsewhere diffuse along the grain boundaries into the pores; grains grow as atoms detach from one grain and join another. Two outcomes are expected. If diffusion on the grain boundaries is fast, pores are extinct before too much grain growth, so that sintering produces a dense, fine-grained ceramic. Alternatively, if

* Corresponding author. Tel.: 001 609 258 0250; fax: 001 609 258 1139; e-mail: suo@princeton.edu

0022–5096/99/$ - see front matter
PII: S0022–5096(98)00093–3

grain boundary migration is fast, pores are unable to keep up, so that the pores separate from the grain boundaries. After being trapped inside the grains, the pores can only be eliminated by lattice diffusion, which is a much slower process than grain boundary diffusion. Furthermore, once free from the pores, the grain boundaries move even more rapidly. Consequently, the separation leads to a porous, coarse-grained ceramic.

Three atomic processes underlie this competition: diffusion on grain boundaries responsible for pore shrinkage, diffusion on pore surfaces for pore motion, and grain boundary migration for grain growth. In an early model, Brook (1969) assumed that pores were spherical, and obtained approximate pore velocity and grain boundary velocity. The separation was assumed to occur when the pore velocity was less than the grain boundary velocity. Although the model was based on an incorrect pore shape, the separation condition showed the correct trend in terms of pore size, grain size, surface mobility, and grain boundary mobility. Hsueh et al. (1982) considered the effects of the pore shapes by studying a pore moving with a grain boundary migrating at a steady velocity. The transient separation processes, however, has never been simulated before.

This paper studies both the steady and transient motion. A pore can change shape and position by evaporation–condensation, surface diffusion, and volume diffusion. Shewmon (1964) discussed the relative importance of these processes and showed that surface diffusion dominates for small pores. Hsueh and Evans (1983) concluded that the contribution of evaporation–condensation to the transport in Al_2O_3 is negligible for all reasonable pore sizes (<10 μm). In this paper, we assume that surface diffusion is the sole process for the pore to adjust its shape and position. Following the previous workers, we focus on the process of separation, and neglect the grain boundary diffusion, so that the volume of the pore remains invariant as it changes shape and position. The effect of grain boundary diffusion may be important; however, its inclusion would require significant development of our finite element program, and will not be studied here.

Rödel and Glaeser (1990) designed a model experiment to study the pore behaviors during grain growth. They used lithography to make holes of a well defined size and spacing on the surface of a plate of sapphire (single crystal Al_2O_3), and then diffusion bonded the sapphire onto a plate of alumina (polycrystalline Al_2O_3). The sapphire–alumina interface was a grain boundary, on which all the holes initially lay. At an elevated temperature, the single crystal grew at the expense of the polycrystal, driven by the total area reduction of the grain boundaries that intersect with the interface. The pores either moved with, or broke away from, the interface. This experiment motivates our three-dimensional and axisymmetric model, as depicted in Fig. 1. A pore sits on a grain boundary (i.e. the sapphire–alumina interface). The pore size is characterized by r_0, the radius of a sphere that has the same volume as the pore. The diameter of the axisymmetric unit is $2R$, which represents pore spacing. For simplicity, we assume that the pore spacing is equal to the grain size in the alumina. A force f_b at the outside edge of the interface represents the force on the interface by the grain boundaries in the alumina. The shapes of the pore and the interface are not prescribed, but evolve according to their own dynamics: the pore moves by atomic diffusion on

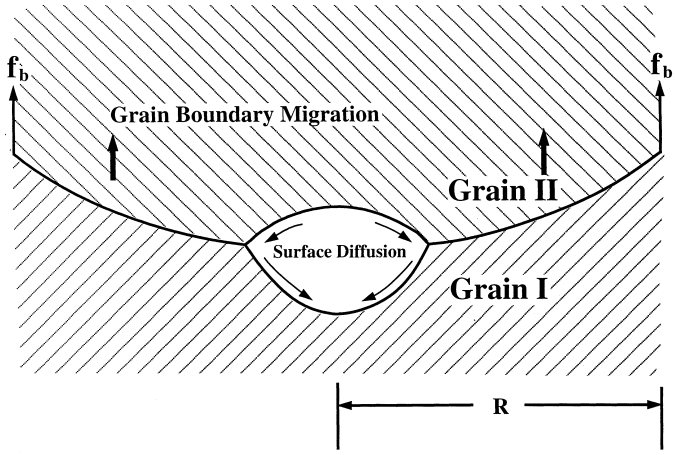

Fig. 1. An axisymmetric model. Grain I grows at the expense of grain II. The pore moves as mass diffuses on the surface. The volume of the pore is $4\pi r_0^3/3$.

its surface, and the interface moves as atoms detach from grain II and attach to grain I.

In their classical work, Herring (1951) and Mullins (1957) used curvature and its gradient to evolve surfaces. In this paper we use this approach to analyse steady state motion. Such an approach, however, has drawbacks in formulating a numerical method to simulate transient motion. Calculating curvature and its derivatives requires that the surfaces be very smooth and have derivatives of several orders. Close attention is needed to ensure that dihedral angles maintain equilibrium values during surface evolution. Recently, a weak statement for surface motion has been formulated; see Suo (1997) and Carter et al. (1997) for reviews. It has weaker requirements on the smoothness of surfaces. On the basis of the weak statement, Sun and Suo (1997a), Sun et al. (1997b), have developed a finite element program for simulating surface motion in two dimensions. Numerical examples have demonstrated that the method can capture intricate details in transient motion. The dihedral angles evolve automatically to their equilibrium values in the first several time steps in simulation. The method readily includes multiple energetic forces and rate processes.

This method can be compared to the computer program Surface Evolver developed by Brakke (1992). In its present version, the Surface Evolver evolves surfaces by a gradient descent method. The simulation does not involve kinetics. It is well known that energetics alone cannot determine the evolution path or final morphology of a structure. The free energy gradient direction differs from the evolution direction. Pore–grain boundary separation process is such an example, where kinetics plays an essential role. In our method, kinetics and energetics together determine the evolution direction. It is hoped that in future our method will be implemented on the geometric setting of the Surface Evolver.

Dimensionality is important to the motion of a pore on a grain boundary. In three dimensions, the force exerted on the pore by a grain boundary is proportional to the

pore radius. However, in two dimensions, where the pore is a circle, the force exerted by the grain boundary is independent of the pore radius. Furthermore, in three dimensions, surfaces have two principal curvatures, which give rise to complex behaviors, as will be evident later. Axisymmetric surface motion has been used to model several phenomena, including spheroidization of a rod shaped particle (Nichols and Mullins, 1976), cavity growth on a grain boundary (Pharr and Nix, 1979), holes in thin films (Srolovitz and Safran, 1986), sintering and coarsening of rows of particles (Cannon and Carter, 1989; Parhami et al., 1998), and the Rayleigh instability of a cylinder (Coleman et al., 1995, 1996). However, no general purpose computer program exists that simulates concomitant surface diffusion and grain boundary migration.

The plan of this paper is as follows. We review the weak statement, and use it to formulate a finite element method for axisymmetric surface motion. We then report the simulations of transient motion of a pore on a grain boundary. More rigorous steady state solutions are obtained and compared with the finite element simulation.

2. Weak statement

We first consider one surface, and then a system of surface and grain boundaries. Imagine two concomitant processes on a solid surface: the solid matter can relocate on the surface by diffusion, and exchange with the surrounding vapor by evaporation–condensation. As will be explained later, evaporation–condensation is included here for numerical convenience. Figure 2 illustrates a solid surface in three dimensions. Denote the unit vector normal to the surface element by $\boldsymbol{n}$. An arbitrary contour lies on the surface, with the curve element dl, and the unit vector $\boldsymbol{m}$ in the surface and normal to the curve element. At a point on the contour, $\boldsymbol{m}$ and $\boldsymbol{n}$ are perpendicular to each other, and both are perpendicular to the tangent vector of the curve at the point. Mass flux $\boldsymbol{J}$ is a vector field tangent to the surface, defined such that $\boldsymbol{J}\cdot\boldsymbol{m}$ is the volume of matter crossing per unit length of the curve per unit time. The mass exchange between the solid and the vapor is represented by flux j, which is the volume of matter added to a unit area of the solid surface per unit time due to evaporation–

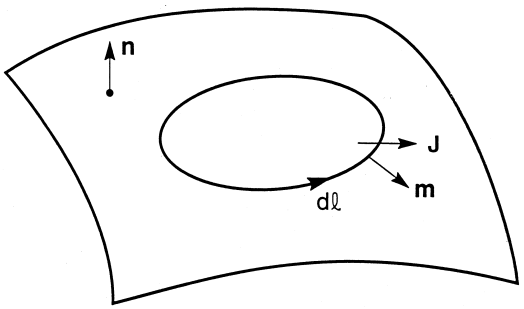

Fig. 2. A surface of a solid in three dimensions.

condensation. Both fluxes $\boldsymbol{J}$ and j change the geometry of the solid. Mass conservation relates the normal velocity of the surface, v_n, to the fluxes of the two matter transport processes:

$$v_n = j - \nabla \cdot \boldsymbol{J}. \tag{1}$$

Here $\nabla \cdot \boldsymbol{J}$ is the surface divergence of $\boldsymbol{J}$.

Define the mass displacement, $\delta \boldsymbol{I}$, as a vector field tangent to the surface, so that $\delta \boldsymbol{I} \cdot \boldsymbol{m}$ is the volume of matter crossing per unit length of the curve. Let δi be the volume of matter added to a unit area of the solid from the vapor. The two kinds of virtual mass displacements $\delta \boldsymbol{I}$ and δi cause a virtual motion of the surface in the direction normal to the surface, δr_n. Mass conservation requires that

$$\delta r_n = \delta i - \nabla \cdot (\delta \boldsymbol{I}). \tag{2}$$

Physically, $\delta \boldsymbol{I}$ and δi represent independent ways to change solid shape. The shape change δr_n relates to the two ways by (2). In numerical simulation, as will be clear below, it is more convenient to treat δr_n and $\delta \boldsymbol{I}$ as independent quantities and subject δi to the constraint (2).

It is of limited use to include anisotropic surface tension in an axisymmetric model. In this paper we will adopt isotropic surface tension. Let γ_S be the surface energy density. The total free energy is

$$G = \gamma_S A_S, \tag{3}$$

where A_S is the area of the surface. The free energy may also include a volumetric term due to the chemical potential difference between atoms in solid and in vapor. The term has been discussed in Suo (1997). In this paper, only negligible amount of evaporation–condensation is allowed so that we do not include this chemical potential difference in G. Thermodynamics requires that the surface evolve to decrease the free energy. However, infinitely many ways of surface motion can decrease the free energy. To determine the actual surface motion, we must specify kinetic processes.

Associated with the virtual motion, the free energy changes by δG. Let $\boldsymbol{F}$ be the free energy reduction associated with a unit volume of matter relocating on the surface per unit distance, and p be the free energy reduction associated with a unit volume of matter deposited to the solid surface from the vapor. Consequently, associated with the virtual motion, the total free energy reduces by

$$\int (\boldsymbol{F} \cdot \delta \boldsymbol{I} + p \delta i) \, \mathrm{d}A = -\delta G. \tag{4}$$

The integral extends over the entire surface area participating in mass transfer. Because $\delta \boldsymbol{I}$ and δi are independent and arbitrary, the weak statement defines the quantities $\boldsymbol{F}$ and p at every point on the surface.

Following Herring (1951), we write the kinetic law for surface diffusion:

$$\boldsymbol{J} = M_S \boldsymbol{F}. \tag{5}$$

The mobility is $M_S = \Omega D \delta / kT$, where Ω is the volume per atom, D the self-diffusivity on the surface, δ the effective thickness of atoms participating in diffusion, k Boltz-

mann's constant, and T the absolute temperature. The kinetic law for evaporation–condensation is (Mullins, 1957)

$$j = m_S p, \tag{6}$$

where m_S is the specific rate of evaporation–condensation.

Substituting (5) and (6) into (4), we obtain that

$$\int \left(\frac{\boldsymbol{J}\delta\boldsymbol{I}}{M_S} + \frac{j\delta i}{m_S} \right) \mathrm{d}A = -\delta G. \tag{7}$$

This is the weak statement for concomitant evaporation–condensation and surface diffusion. In finite element implementation, it is convenient to use $\delta\boldsymbol{I}$ and δr_n as the independent variables. Eliminating j and δi in (7) by using (1) and (2), we obtain that

$$\int \left\{ \frac{\boldsymbol{J}\cdot\delta\boldsymbol{I}}{M_S} + \frac{(v_n + \nabla\cdot\boldsymbol{J})[\delta r_n + \nabla\cdot(\delta\boldsymbol{I})]}{m_S} \right\} \mathrm{d}A = -\delta G. \tag{8}$$

In this form, the weak statement only involves two virtual fields, δr_n and $\delta\boldsymbol{I}$. They vary independently, subject to no constraint. For a pore migrating with the grain boundary, we do not consider evaporation–condensation on the pore surface. We let m_S be a very small number, so that the second term in the integral enforces the mass conservation condition in simulation.

For a system of surfaces and grain boundaries, the total free energy is

$$G = \gamma_S A_S + \gamma_B A_B, \tag{9}$$

where γ_B is the grain boundary energy density, and A_B the total grain boundary area. The grain boundary migrates as atoms detach from one side and attach to the other side. The kinetic law for grain boundary migration is similar to (6), relating the normal grain boundary velocity v_n to the driving pressure p_B:

$$v_n = m_B p_B, \tag{10}$$

where m_B is the grain boundary mobility. The virtual motion of the grain boundaries and surfaces change the total free energy by δG. Equation (8) is extended to

$$\int \left\{ \frac{\boldsymbol{J}\cdot\delta\boldsymbol{I}}{M_S} + \frac{(v_n + \nabla\cdot\boldsymbol{J})[\delta r_n + \nabla\cdot(\delta\boldsymbol{I})]}{m_S} \right\} \mathrm{d}A + \int \left\{ \frac{v_n \delta r_n}{m_B} \right\} \mathrm{d}A = -\delta G. \tag{11}$$

The first integral is over the surfaces between the solid and the vapor, and the second over all the grain boundaries.

3. Axisymmetric finite elements

The procedure of formulating a finite element is the same as in Sun and Suo (1997a), Sun et al. (1997b). Here we emphasize the aspects specific to axisymmetric surfaces. An axisymmetric surface is generated by rotating a plane curve around an axis lying

on the same plane. We divide the generating curve into many small straight elements. The motions of the nodes describe the motion of the surface. Each node on the plane curve represents a circle on the surface in three dimensions. Figure 3 shows one element with nodes (x_1, y_1) and (x_2, y_2). The element has length l and slope θ; the local coordinate, s, is measured from the mid-point of the element. Let I_1, I_2, I_m be the mass displacements at the two nodes and the mid-point of the element. For each surface element, the generalized coordinates are

$$\boldsymbol{q}^e = [x_1 \quad y_1 \quad I_1 \quad x_2 \quad y_2 \quad I_2 \quad I_m]^T. \tag{12a}$$

Let $\dot{x}_1$, $\dot{y}_1$, $\dot{x}_2$, $\dot{y}_2$ be the nodal velocities of the element, and J_1, J_2 and J_m be the fluxes at the two nodes and the mid-point of the element. The generalized velocities are

$$\dot{\boldsymbol{q}}^e = [\dot{x}_1 \quad \dot{y}_1 \quad J_1 \quad \dot{x}_2 \quad \dot{y}_2 \quad J_2 \quad J_m]^T. \tag{12b}$$

On the element, interpolate the virtual displacement and actual velocity linearly:

$$\delta r_n = N_1 \delta x_1 + N_2 \delta y_1 + N_3 \delta x_2 + N_4 \delta y_2$$

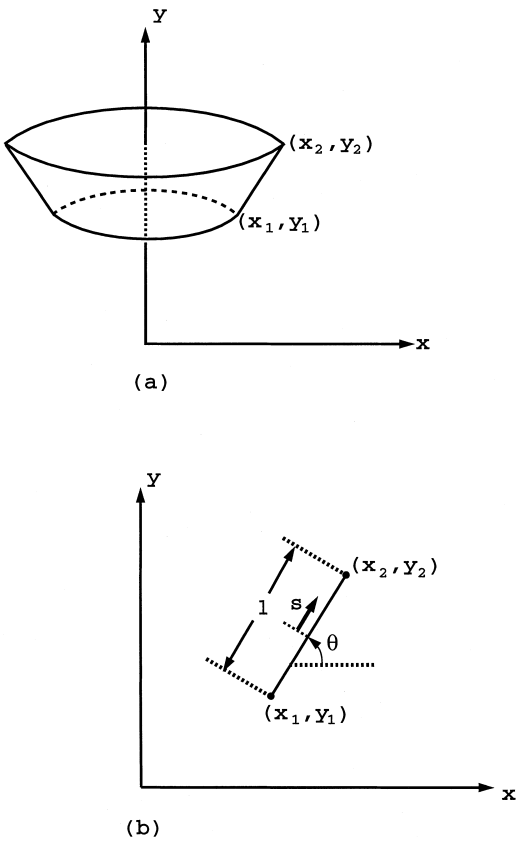

Fig. 3. An axisymmetric element in three dimensions (a) and in a plane (b).

$$v_n = N_1\dot{x}_1 + N_2\dot{y}_1 + N_3\dot{x}_2 + N_4\dot{y}_2 \tag{13}$$

with the interpolation coefficients being

$$N_1 = -\left(\frac{1}{2} - \frac{s}{l}\right)\sin\theta, \quad N_2 = \left(\frac{1}{2} - \frac{s}{l}\right)\cos\theta,$$

$$N_3 = -\left(\frac{1}{2} + \frac{s}{l}\right)\sin\theta, \quad N_4 = \left(\frac{1}{2} + \frac{s}{l}\right)\cos\theta. \tag{14}$$

Interpolate the virtual mass displacement and actual mass flux quadratically:

$$\delta I = Q_1\delta I_1 + Q_2\delta I_2 + Q_3\delta I_m,$$
$$J = Q_1 J_1 + Q_2 J_2 + Q_3 J_m, \tag{15}$$

with the interpolation coefficients being

$$Q_1 = \frac{s}{l}\left(1 - \frac{2s}{l}\right), \quad Q_2 = \frac{s}{l}\left(1 + \frac{2s}{l}\right), \quad Q_3 = 1 - \left(\frac{2s}{l}\right)^2. \tag{16}$$

For each element, the integral over the surface in (11) gives a bilinear form

$$(\delta\boldsymbol{q}^e)^T\boldsymbol{H}^e\boldsymbol{q}^e, \tag{17}$$

where $\boldsymbol{H}^e$ is a 7×7 matrix, the components of which are given in the Appendix. The corresponding integral in (11) for one grain boundary element takes a similar form as (17), with $\boldsymbol{q}^e$ only having four components and $\boldsymbol{H}^e$ a 4×4 matrix, whose components are also listed in the Appendix.

The right-hand side of (11), δG, is a sum over all the elements. For one element, the surface area is $A = \pi(x_1 + x_2)l$. Consequently, the free energy reduction of the element is

$$-\gamma\delta A = f_1\delta x_1 + f_2\delta y_1 + f_3\delta x_2 + f_4\delta y_2, \tag{18}$$

where $\gamma = \gamma_S$ for a surface element or $\gamma = \gamma_B$ for a grain boundary element. The force components acting on the two nodes due to the element surface tension are

$$\begin{bmatrix} f_1 \\ f_2 \\ f_3 \\ f_4 \end{bmatrix} = \pi\gamma \begin{bmatrix} -l + (x_1 + x_2)\cos\theta \\ (x_1 + x_2)\sin\theta \\ -l - (x_1 + x_2)\cos\theta \\ -(x_1 + x_2)\sin\theta \end{bmatrix}. \tag{19}$$

Because G defined by (9) varies as the shape varies, we only have driving forces associated with the motion of the coordinates. No driving forces are associated with δI_1, δI_2, δI_m.

Assemble all the nodal velocities and fluxes into a column $\dot{\boldsymbol{q}}$, and the corresponding virtual movements and mass displacements into a column $\delta\boldsymbol{q}$. Assemble all the nodal

forces into a column $\boldsymbol{f}$ and arrange their sequence such that $-\delta G = \delta \boldsymbol{q}^{\mathrm{T}} \boldsymbol{f}$. Sum over all the elements, (11) becomes

$$\delta \boldsymbol{q}^{\mathrm{T}} \boldsymbol{H} \dot{\boldsymbol{q}} = \delta \boldsymbol{q}^{\mathrm{T}} \boldsymbol{f}. \tag{20}$$

Equation (20) holds for any virtual motion $\delta \boldsymbol{q}$, so that

$$\boldsymbol{H} \dot{\boldsymbol{q}} = \boldsymbol{f}. \tag{21}$$

The matrix $\boldsymbol{H}$ is symmetric and positive-definite, which we call the viscosity matrix. The components of the viscosity matrix $\boldsymbol{H}$ and force vector $\boldsymbol{f}$ depend on $\boldsymbol{q}$. Consequently, equation (21) is a set of nonlinear ordinary differential equations that govern the generalized coordinates as a function of time. From (21), we can see that the velocity direction usually differs from the direction of the generalized force, i.e., gradient of free energy. Equation (21) is integrated numerically to evolve the surfaces.

4. Transient process

Our simulation model has been discussed in the Introduction (Fig. 1). The model has dimensionless parameters: $m_{\mathrm{B}} r_0^2 / M_{\mathrm{S}}$, $\gamma_{\mathrm{B}}/\gamma_{\mathrm{S}}$, $f_{\mathrm{B}}/\gamma_{\mathrm{S}}$, R/r_0. The unit of time in the simulation is $r_0^4 / M_S \gamma_S$.

Figure 4 shows the simulation under condition $m_{\mathrm{B}} r_0^2 / M_{\mathrm{S}} = 1$, $R/r_0 = 5$, $f_{\mathrm{b}}/\gamma_{\mathrm{S}} = 0.5$ and $\gamma_{\mathrm{B}}/\gamma_{\mathrm{S}} = 1$. To mimic the holes on the sapphire surface made by lithography (Rödel and Glaeser, 1990), we assume the initial condition that, at $t = 0$, the pore is a cylindrical disk. The pore evolves to a rounded shape quickly. After some time it approaches to a steady state shape, and moves at a constant velocity with the grain boundary. Note the vertical coordinates to see the motion. The dihedral angles at the triple junction automatically reach their equilibrium values in several time steps in the beginning of the simulation and are kept thereafter. As shown by Suo (1997), the equilibrium dihedral angles are the natural boundary conditions enforced automatically by the weak statement. They are the output of the simulation, not the input. This feature considerably simplifies the computer code.

In Figure 5(a), the mobility ratio is increased to $m_{\mathrm{B}} r_0^2 / M_{\mathrm{S}} = 10$, and the other parameters are kept the same as in Fig. 4. In reality the mobility ratio may be changed by adding suitable impurities or by changing temperature. The grain boundary now migrates so fast that the pore is unable to keep up. The pore separates from the grain boundary and is left inside the grain. Afterwards the pore evolves to a sphere by surface diffusion. In simulation, when the triple junction is very close to the rotating axis and the pinch-off is imminent, the program allows the grain boundary to break. Because the pinch-off process happens very fast, the programming details have little effect on the overall behavior.

Figure 5(b) shows the effect of pore spacing. Compared with Fig. 4, the only parameter changed is R/r_0. In this case, the pore also detaches from the grain boundary. In reality $2R$ can be interpreted as the grain size of the smaller neighboring grain

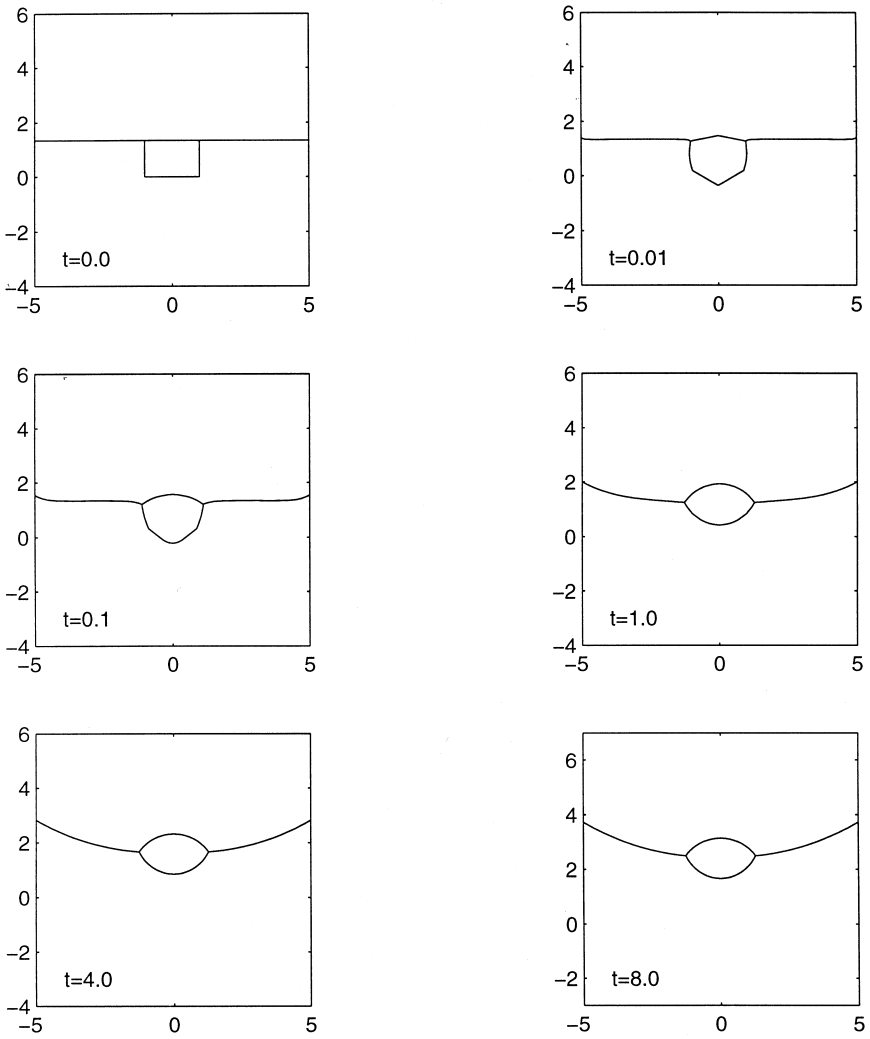

Fig. 4. Pore–grain boundary attachment. A time series of a pore moving with a grain boundary ($\gamma_B/\gamma_S = 1$, $f_b/\gamma_S = 0.5$, $m_B r_0^2/M_S = 1$, $R/r_0 = 5$).

which is next to the growing grain. A lot of small grains next to a big grain means a large driving force for grain boundary migration.

5. Steady state motion

As we have seen above, under certain conditions, the pore and the grain boundary can migrate at the same velocity. The steady state pore shape was studied by Huesh

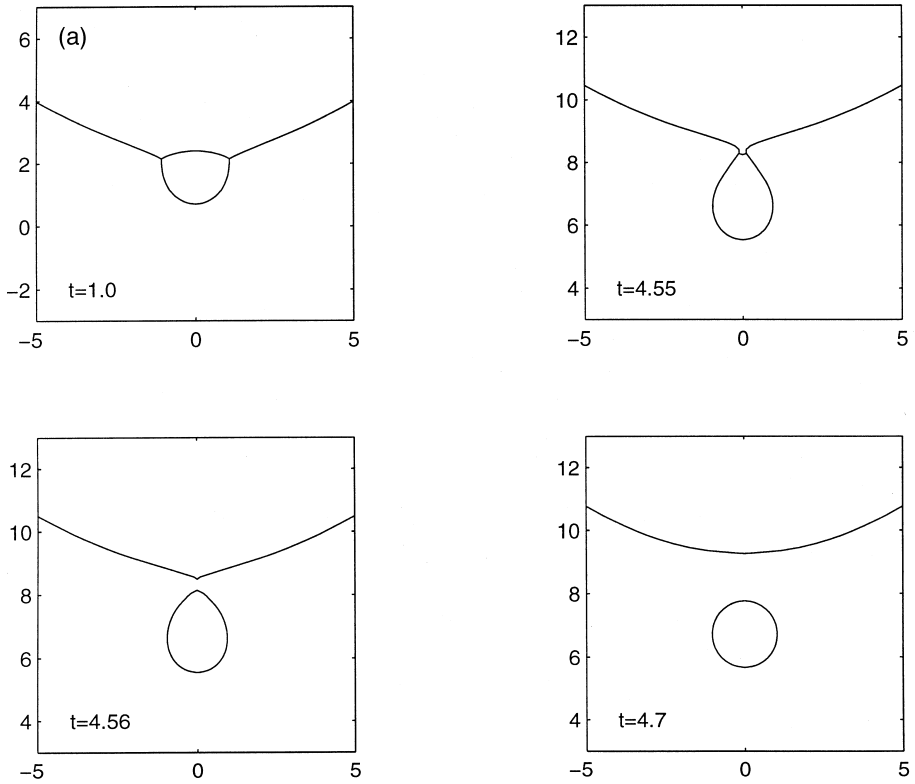

Fig. 5. Pore–grain boundary separation. (a) Effect of mobility: $m_B r_0^2/M_S = 10$, $R/r_0 = 5$; (b) Effect of spacing: $m_B r_0^2/M_S = 1$, $R/r_0 = 1.5$.

et al. (1982), whose results were then used by Rödel and Glaeser (1990) to estimate the surface diffusion coefficient of alumina from experimental data. We tried to use the same solutions to check our finite element program, but found large discrepancies. Subsequently, we decided to derive the steady state solutions more rigorously. We found several surprising features of the solutions.

Figure 6 shows the geometry. First we consider the pore motion alone. The grain boundary comes in by the parameter γ_B/γ_S, which fixes the equilibrium dihedral angle ψ_e according to

$$\cos(\psi_e/2) = \gamma_B/2\gamma_S. \tag{22}$$

The limiting case, $\gamma_B/\gamma_S \to 0$, can be solved analytically. The surface tension of the pore, γ_S, is so large that the pore retains a spherical shape as it moves. Note that the dihedral angle $\psi_e = 180^\circ$, and the grain boundary approaches the pore surface perpendicularly. The neck radius a relates to the pore radius r_0 as $a = r_0 \cos\phi$. Consequently, the grain boundary exerts a force on the pore,

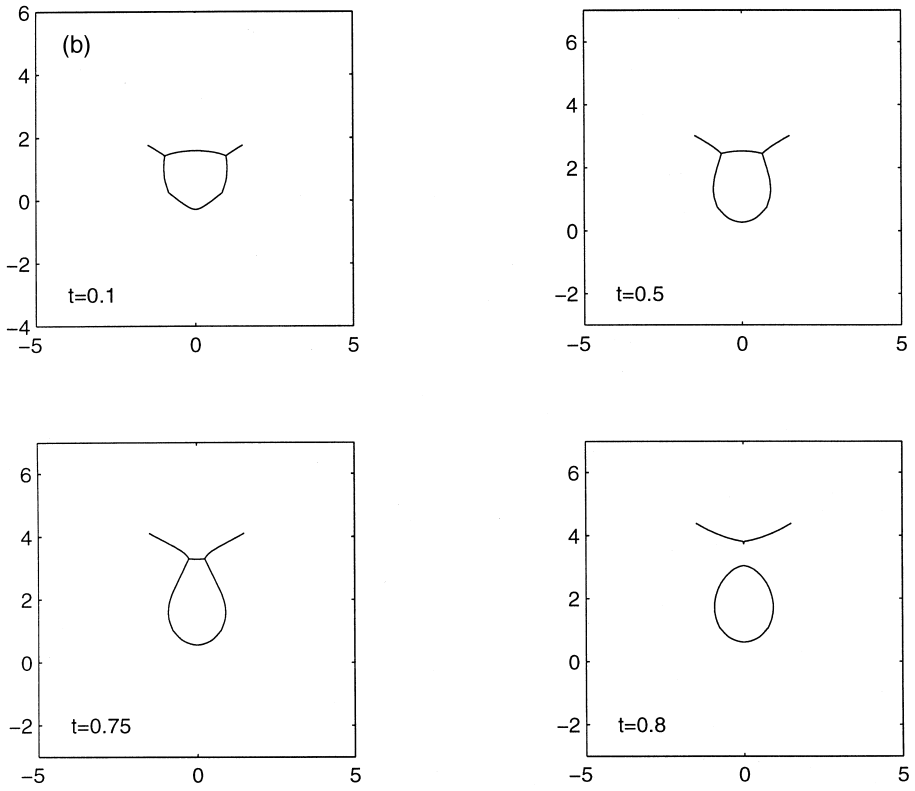

Fig. 5 (*continued*)

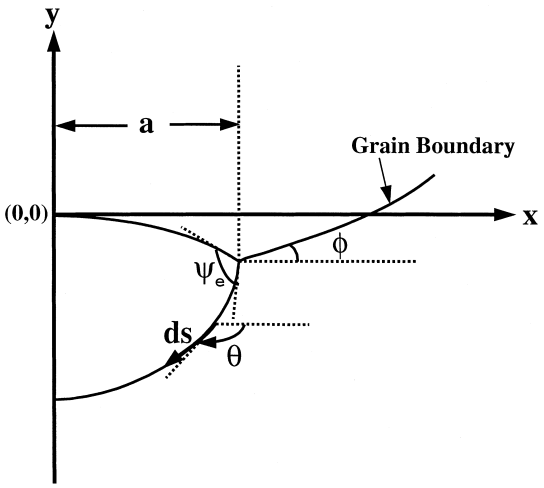

Fig. 6. Geometry of a pore in a steady state.

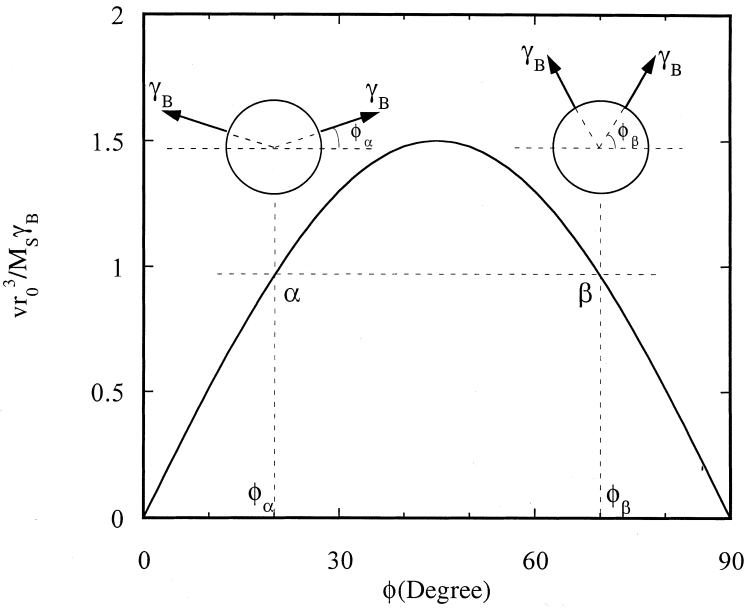

Fig. 7. Pore velocity as a function of dragging angle ($\gamma_B/\gamma_S = 0$, spherical pore). Two configurations, α and β, correspond to each velocity.

$$F = 2\pi r_0 \gamma_B \sin\phi \cos\phi. \tag{23}$$

Suo (1997, p. 263) derived the exact velocity of a sphere moving by surface diffusion:

$$v = 3M_S F/2\pi r_0^4. \tag{24}$$

This relation has the same form as the approximate solution derived by Shewmon (1964), but a different numerical factor. A combination of (23) and (24) gives that

$$v = \frac{3M_S\gamma_B}{2r_0^3}\sin 2\phi. \tag{25}$$

Figure 7 shows the normalized pore velocity as a function of the dragging angle ϕ. Observe that, for a given normalized velocity, there exist two configurations. The nonuniqueness is understood as follows. Configuration α has a large neck radius and a small dragging angle; configuration β has a small neck radius and a large dragging angle. Consequently, the two configurations have the same dragging force, and therefore the same velocity. (This nonuniqueness does not occur in two dimensions, where the pore is a circle and the force per unit length is $2\gamma_B \sin\phi$.) At $\phi = \pi/4$, the pore velocity reaches the maximum,

$$v_{max} = \frac{3\gamma_B M_S}{2r_0^3}. \tag{26}$$

Brook (1969) used the maximum velocity (without the factor 3/2) to derive an approximate separation condition.

We next consider the general case where $\gamma_B/\gamma_S > 0$ and the dihedral angle $\psi_e < 180^\circ$. The pore shape is no longer spherical, and must be solved as a part of the problem. As the pore moves at the velocity v in Fig. 6, mass must diffuse on the surface. Consider a circle of radius x on the surface. The volume of the mass moving across the circle per unit time is $2\pi xJ$. Mass conservation requires that

$$2\pi xJ = \pi x^2 v.$$

Let κ be the sum of the principal curvatures of the surface, and s the arc length of the curve starting from the north pole. According to Herring (1951), the flux relates to the curvature gradient along the surface:

$$J = -M_S\gamma_S \, \mathrm{d}\kappa/\mathrm{d}s.$$

A combination of the above two equations gives that

$$\frac{\mathrm{d}\kappa}{\mathrm{d}s} = -\frac{x}{2L^3},$$

where L is a length scale defined by $L^3 = M_S\gamma_S/v$. For an axisymmetric surface, the sum of the principal curvatures is (Struik, 1988)

$$\kappa = \frac{\mathrm{d}\theta}{\mathrm{d}s} + \frac{\sin\theta}{x},$$

where θ is the tangential angle of the curve. The set of ordinary equations are

$$\frac{\mathrm{d}x}{\mathrm{d}s} = \cos\theta, \quad \frac{\mathrm{d}y}{\mathrm{d}s} = \sin\theta, \quad \frac{\mathrm{d}\theta}{\mathrm{d}s} = \kappa - \frac{\sin\theta}{x}, \quad \frac{\mathrm{d}\kappa}{\mathrm{d}s} = -\frac{x}{2L^3}. \tag{27a}$$

The first three equations are geometric relations. Because of symmetry, we just calculate the curve at the one side of the rotating axis. Instead of using the x coordinate as the independent variable, here we use the arc length s. Consequently, the ODEs can deal with curves with a tangential vector perpendicular to the x-axis. If x were the independent variable, this would be a singular point. Normalize all lengths in (27a) by the neck radius, a. The first three equations in (27a) retain the same form, but the last equation becomes (in terms of dimensionless quantities)

$$\frac{\mathrm{d}\kappa}{\mathrm{d}s} = -\frac{1}{2}\left(\frac{a}{L}\right)^3 x. \tag{27b}$$

In the normalized coordinate, $x = 1$ at the neck.

Equations (27) are nonlinear ODEs that govern x, y, θ and κ as functions of s. It is inappropriate to linearize them for the present problem, so we integrate them in the present form. For given values of a/L and γ_B/γ_S, we solve ODEs (27) by a shooting method. At the north pole, where $x = y = \theta = 0$, we guess a value of κ. This defines an initial value problem. Integrate (27) to the triple junction ($x = 1$). Keep x, y,

κ continuous (i.e. continuous chemical potential), but change θ according to the equilibrium dihedral angle, $\Delta\theta = -(\pi - \psi_e)$. Integrate (27) further to the south pole, and see if the curve can hit the y-axis at $\theta = -\pi$. The shooting is combined with searching and bisection to search for multiple solutions. After obtaining a solution of the curve, we compute the pore volume and equate it to $4\pi r_0^3/3$ to obtain r_0. Finally renormalize all the lengths by r_0, so that all pores have the same volume.

The problem has two dimensionless parameters: the normalized velocity $vr_0^3/M_S\gamma_B$, and the surface tension ratio γ_B/γ_S. Corresponding to one pair of the parameters, we find many steady state solutions. Figure 8 shows six pores all having $vr_0^3/M_S\gamma_B = 0.47$ and $\gamma_B/\gamma_S = 1$. The pair I_α and I_β have one cell; II_α and II_β have two; and III_α and III_β have three. We also find solutions with four cells, five cells, etc. The

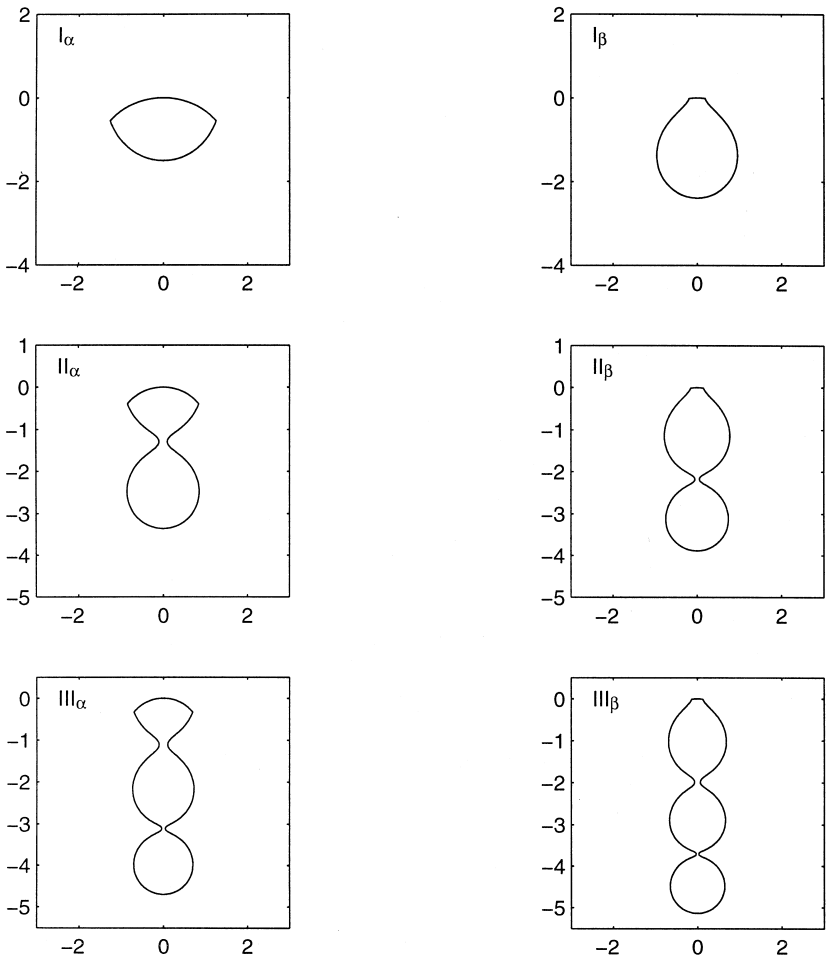

Fig. 8. Different pore shapes for given parameters $vr_0^3/M_S\gamma_B = 0.47$ and $\gamma_B/\gamma_S = 1$.

pair I_α and I_β indicate that the solution is nonunique even for pores with one cell. The reason for this nonuniqueness is analogous to that for the spherical pore given before.

Figure 9 shows part of the solution structure for $\gamma_B/\gamma_S = 1$ (i.e., $\psi_e = 120^\circ$), where the dragging angle (9a) and neck radius (9b) are plotted as functions of the normalized

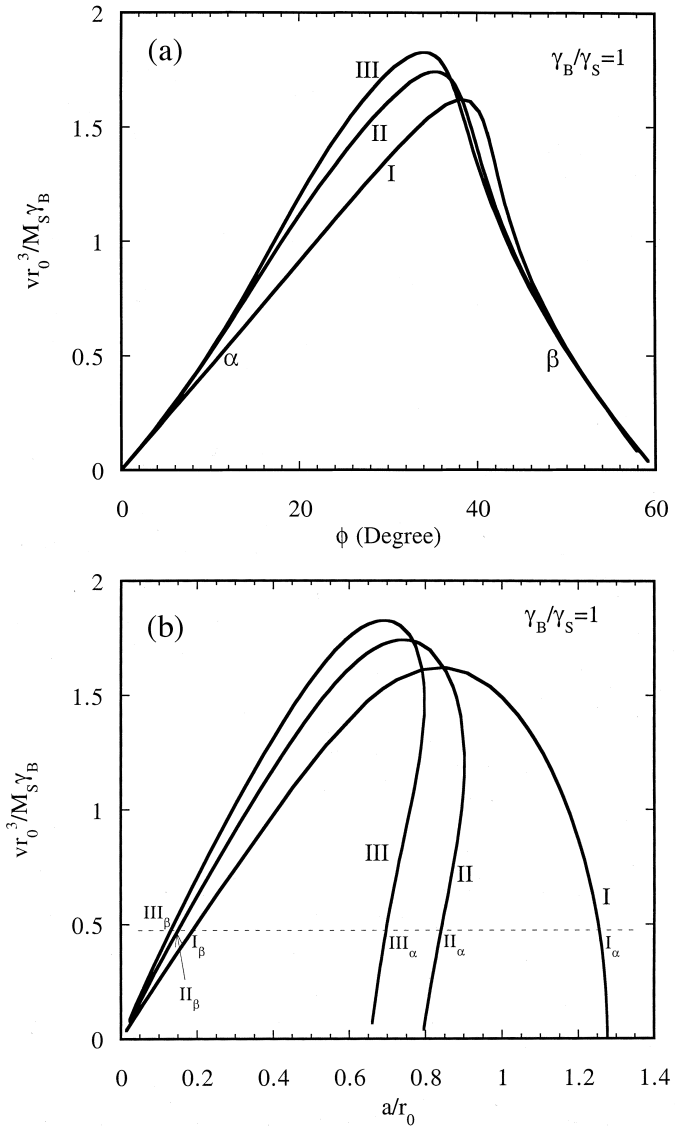

Fig. 9. Steady state solution structure for $\gamma_B/\gamma_S = 1$. (a) Dragging angle as a function of normalized velocity; (b) Neck radius as a function of normalized velocity. Curve I represents the solutions with one cell, II the solutions with two cell, and III the solutions with three cells. Points marked in (b) correspond to the six pores in Fig. 8.

velocity. We just plot the solutions with one, two, and three cells, represented by curve I, II and III, respectively. Along each curve, the pore shape changes continuously with the normalized velocity. The points marked in Fig. 9(b) correspond to the six pores in Fig. 8.

The above qualitative behaviors are also observed for smaller values of γ_B/γ_S. In the limiting case, $\gamma_B/\gamma_S \to 0$, in addition to the single sphere solutions discussed above, a row of smaller touching spheres is also a solution, corresponding to the limiting case of a many-cell solution shown in Fig. 8. For larger γ_B/γ_S values, however, the behavior can be different. Figure 10 shows the solution structure for $\gamma_B/\gamma_S = \sqrt{3}$ (i.e. $\psi_e = 60^\circ$). Now the one-cell solutions can smoothly change to many-cell solutions.

Pores with two or more cells have large surface areas for a given pore volume; they are expected to be unstable. We next focus on pores with only one cell. Figure 11 compares steady state solutions with finite element results. The solid lines are the ODE solutions. The circles (for $\gamma_B/\gamma_S = 1$) and triangles (for $\gamma_B/\gamma_S = \sqrt{3}$) are from finite element simulations, which, starting from some initial pore shapes, after transient motion, have settled to steady states. The finite element results agree well with the ODE solutions. Our finite element simulations, however, cannot reach parts of the curves corresponding to configuration β in Fig. 7 and I_β in Fig. 8. We tentatively conclude that the β solutions are unstable, and the α solutions are stable. More evidence will be given below. Our numerical values are very different from those in Hsueh et al. (1982). Apparently their numerical procedure was inadequate.

For a given γ_B/γ_S, there exists a maximum steady state velocity for one-cell pores. Hsueh et al. (1982) also reported the maximum steady state velocity, obtained when their ODE solutions diverged, which are very different from ours. Figure 12(a) shows

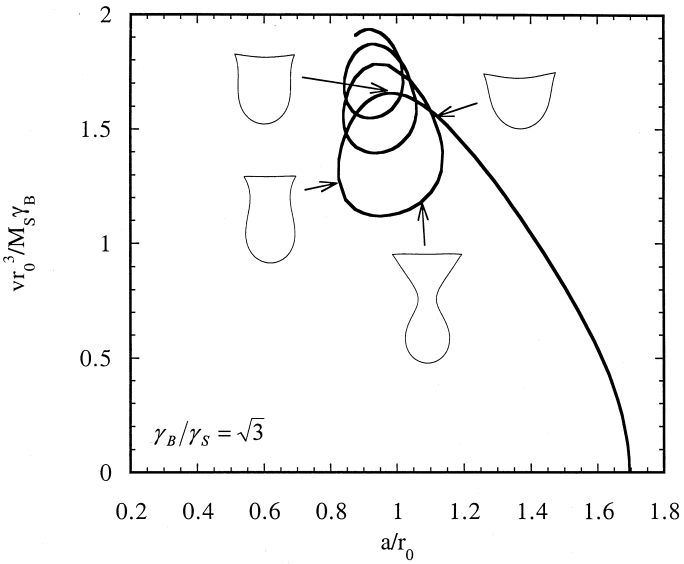

Fig. 10. Solution structure for $\gamma_B/\gamma_S = \sqrt{3}$.

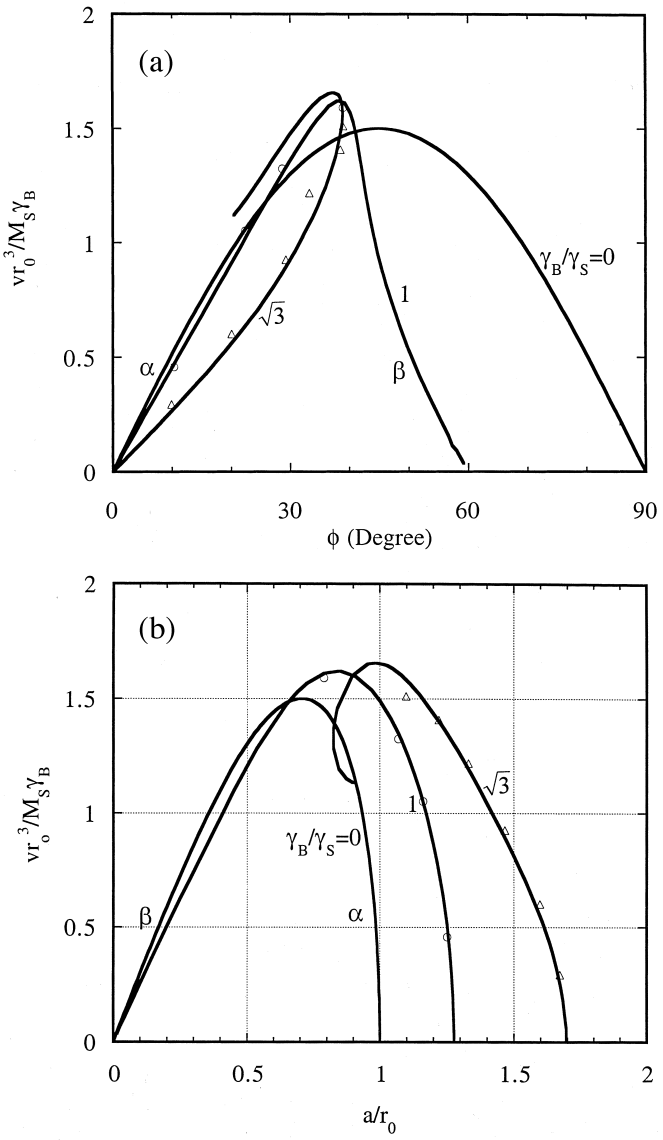

Fig. 11. Comparison of the steady state solutions and the finite element results. (a) Normalized velocity as a function of dragging angle; (b) Normalized velocity as a function of the neck radius. Solid lines are results from the solution of the ODEs; open circles and triangles are the finite element solutions. Finite element simulation cannot reach the β solutions.

that the maximum steady state velocity weakly depends on the surface energy, γ_S, so that the expression (26) is a good approximation for any value of γ_B/γ_S. Also note in Fig. 12(b) that the dragging force at which the maximum velocity occurs depends

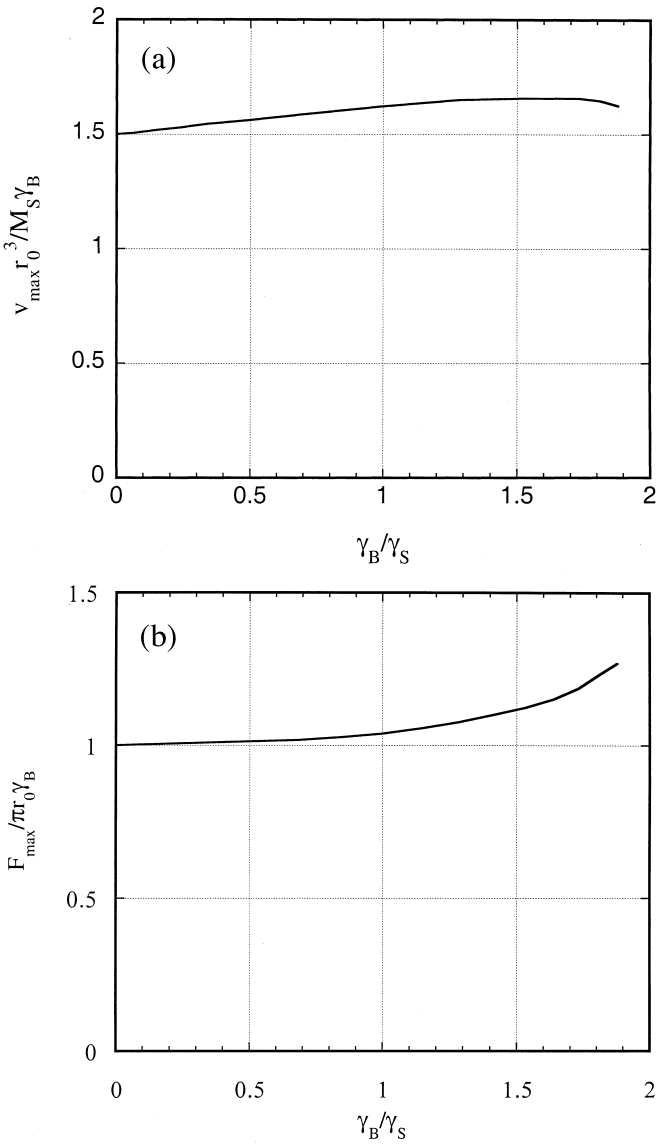

Fig. 12. (a) Maximum pore velocity as a function of γ_B/γ_S. (b) Dragging force at the maximum pore velocity as a function of γ_B/γ_S.

weakly on γ_B/γ_S. As these quantities enter the Brook (1969) model, we conclude that the parameter γ_B/γ_S, i.e., the pore shape, has little effect on the pore–grain boundary separation condition.

All the above results do not depend on the details in the grain boundary movement. The shape of the grain boundary in steady state can also be obtained by solving

ODEs. The first three equations in (27a) still apply. The mean curvature of a grain boundary relates to the velocity as $v\cos\theta = m_B\gamma_B\kappa$. Consequently, the ODEs for the steady state motion of the grain boundary are

$$\frac{dx}{ds} = \cos\theta, \quad \frac{dy}{ds} = \sin\theta, \quad \frac{d\theta}{ds} = \frac{v\cos\theta}{m_B\gamma_B} - \frac{\sin\theta}{x}. \tag{28}$$

We can integrate the ODEs (28) from $x = a$ to $x = R$. The initial tangential angle is ϕ, obtained from the steady state solution for the pore. The force at the edge of the unit is obtained from $f_b = \gamma_B \sin\theta_e$, where θ_e is the tangential angle of the grain boundary at the edge. Figure 13 shows the relation between the dragging force and the steady state velocity for $\gamma_B/\gamma_S = 1$. Both α and β solutions are shown. The open circles are from the finite element simulations. Again, the finite element results agree well with the solutions of the ODEs. There exists a maximum value for the dragging force for each case. If the dragging force exceeds the maximum value, there is no steady state solution.

As stated above, our finite element simulations cannot reach the β solutions (Fig. 11). This suggests that the β solutions be unstable. To further demonstrate this, we choose the initial pore shape I_β in Fig. 8, which is reproduced in Fig. 14(a). The shapes of the pore and the grain boundary are from the steady state solution integrated from the ODEs. Figure 14(b)–(d) show the time sequence of the pore obtained from the finite element simulation. In the simulation, we did not explicitly prescribe any perturbation; the perturbation is due to numerical approximation. Clearly the pore

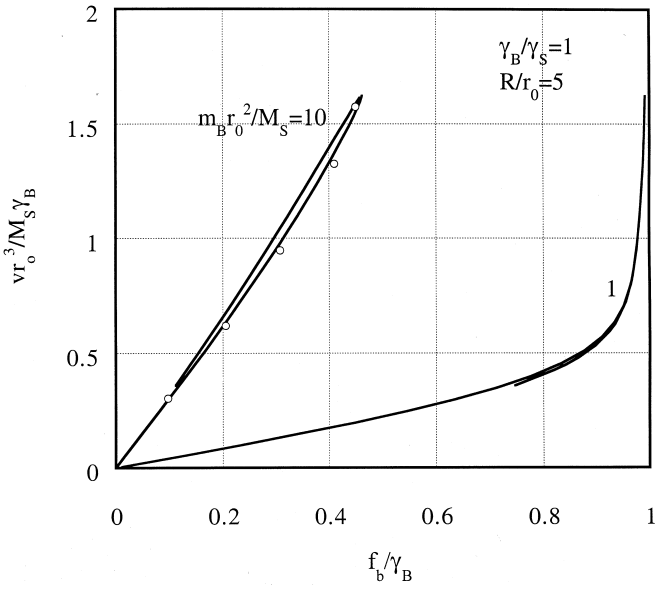

Fig. 13. Normalized velocity as a function of the dragging force. Solid lines are results from the solution of ODEs. Open circles are the finite element solution.

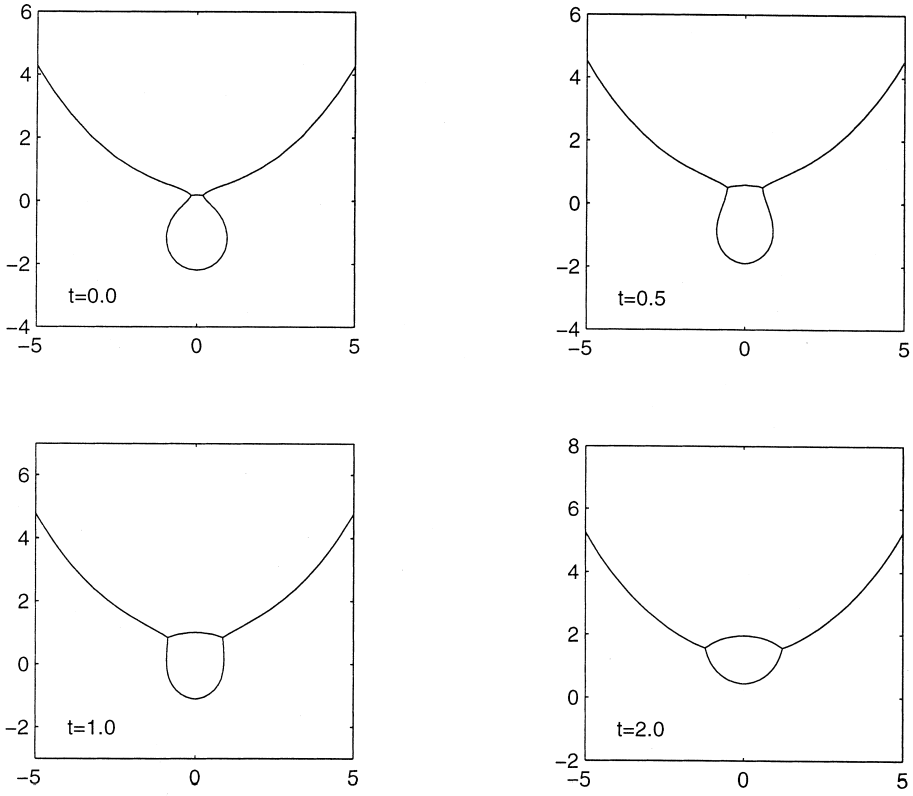

Fig. 14. Stability test of an ODE solution. A pore starts as a β solution and then evolves to an α solution.

does not move in the shape given by the initial condition. Instead, it undergoes a large shape change, and evolves to another steady state similar to Fig. 8 (I_α). This indicates that the initial steady state solution I_β is unstable.

6. Concluding remarks

We formulated a finite element method for simulating three-dimensional axisymmetric surface motion with combined surface diffusion and grain boundary migration. A numerical example, pore–grain boundary separation, demonstrated the capability of the method and the program. We also compared the steady state solutions obtained from finite element simulation with those obtained from a set of ordinary differential equations. They agree well when the solutions are stable. The steady state solutions obtained here greatly improved the ones in the literature. In particular, we found that the maximum velocity for a spherical pore is a good approximation for nonspherical pores, and the dihedral angle should have little effect on pore–grain

boundary separation condition. Our finite element simulation indicated that some of the steady state solutions are unstable. Further study is needed to determine the exact condition for stability. Our finite element program can also simulate other phenomena that can be modeled by axisymmetric surface motion.

Acknowledgements

The work is supported by the National Science Foundation Grant MSS92-58115, and by the Institute for Materials Research and Engineering, Singapore.

Appendix

Let $C=\cos\theta$, $S=\sin\theta$. The surface element viscosity matrix $\boldsymbol{H}^{e}$ is a 7×7 symmetric matrix with element

$$H_{11}=\frac{\pi lS^2(10x_1^3+6x_1^2x_2+3x_1x_2^2+x_2^3)}{30m_S}$$

$$H_{12}=-\frac{\pi lCS(10x_1^3+6x_1^2x_2+3x_1x_2^2+x_2^3)}{30m_S}$$

$$H_{13}=\frac{\pi S(4x_1+x_2)(-2Clx_1+7x_1^2+2x_1x_2+x_2^2)}{30m_S}$$

$$H_{14}=\frac{\pi lS^2(2x_1^3+3x_1^2x_2+3x_1x_2^2+2x_2^3)}{30m_S}$$

$$H_{15}=-\frac{\pi lCS(2x_1^3+3x_1^2x_2+3x_1x_2^2+2x_2^3)}{30m_S}$$

$$H_{16}=\frac{\pi S(Clx_1^2+4x_1^3-3x_1^2x_2-Clx_2^2-6x_1x_2^2-5x_2^3)}{30m_S}$$

$$H_{17}=\frac{2\pi S(-2Clx_1^2-8x_1^3-2Clx_1x_2-3x_1^2x_2-Clx_2^2+x_2^3)}{15m_S}$$

$$H_{22}=\frac{\pi lC^2(10x_1^3+6x_1^2x_2+3x_1x_2^2+x_2^3)}{30m_S}$$

$$H_{23}=\frac{\pi C(4x_1+x_2)(2Clx_1-7x_1^2-2x_1x_2-x_2^2)}{30m_S}$$

$$H_{24}=-\frac{\pi lCS(2x_1^3+3x_1^2x_2+3x_1x_2^2+2x_2^3)}{30m_S}$$

$$H_{25}=\frac{\pi lC^2(2x_1^3+3x_1^2x_2+3x_1x_2^2+2x_2^3)}{30m_S}$$

$$H_{26} = -\frac{\pi C(Clx_1^2+4x_1^3-3x_1^2x_2-Clx_2^2-6x_1x_2^2-5x_2^3)}{30m_S}$$

$$H_{27} = \frac{2\pi C(2Clx_1^2+8x_1^3+2Clx_1x_2+3x_1^2x_2+Clx_2^2-x_2^3)}{15m_S}$$

$$H_{33} = \frac{\pi l(7x_1+x_2)}{30M_S} + \frac{\pi(7C^2l^2x_1x_1-46Clx_1^2+79x_1^3+C^2l^2x_2-12Clx_1x_2+39x_1^2x_2 - 2Clx_2^2+15x_1x_2^2+7x_2^3)}{30m_Sl}$$

$$H_{34} = \frac{\pi S(-Clx_1^2+5x_1^3+6x_1^2x_2+Clx_2^2+3x_1x_2^2-4x_2^3)}{30m_S}$$

$$H_{35} = -\frac{\pi C(-Clx_1^2+5x_1^3+6x_1^2x_2+Clx_2^2+3x_1x_2^2-4x_2^3)}{30m_S}$$

$$H_{36} = -\frac{\pi l(x_1+x_2)}{30M_S} + \frac{\pi(x_1+x_2)(-C^2l^2-2Clx_1+13x_1^2+2Clx_2-16c_1x_2+13x_2^2)}{30m_Sl}$$

$$H_{37} = \frac{2\pi lx_1}{15M_S} + \frac{2\pi(C^2l^2x_1+2Clx_1^2-23x_1^3-2Clx_1x_2-9x_1^2x_2-3x_1x_2^2-5x_2^3)}{15m_Sl}$$

$$H_{44} = \frac{\pi lS^2(x_1^3+3x_1^2x_2+6x_1x_2^2+10x_2^3)}{30m_S}$$

$$H_{45} = -\frac{\pi lCS(x_1^3+3x_1^2x_2+6x_1x_2^2+10x_2^3)}{30m_S}$$

$$H_{46} = -\frac{\pi S(x_1+4x_2)(x_1^2+2Clx_2+2x_1x_2+7x_2^2)}{30m_S}$$

$$H_{47} = \frac{2\pi S(-Clx_1^2-x_1^3-2Clx_1x_2-2Clx_2^2+3x_1^2x_2+8x_2^3)}{15m_S}$$

$$H_{55} = \frac{\pi lC^2(x_1^3+3x_1^2x_2+6x_1x_2^2+10x_2^3)}{30m_S}$$

$$H_{56} = \frac{\pi C(x_1+4x_2)(x_1^2+2Clx_2+2x_1x_2+7x_2^2)}{30m_S}$$

$$H_{57} = \frac{2\pi C(Clx_1^2+x_1^3+2Clx_1x_2+2Clx_2^2-3x_1x_2-8x_2^3)}{15m_S}$$

$$H_{66}=\frac{\pi l(x_1+7x_2)}{30M_S}+\frac{\pi(C^2l^2x_1+2Clx_1^2+7x_1^3+7C^2l^2x_2+12Clx_1x_2+15x_1^2x_2+46Clx_2^2+39x_1x_2^2+79x_2^3)}{30m_Sl}$$

$$H_{67}=\frac{2\pi lx_2}{15M_S}+\frac{2\pi(-5x_1^3+C^2l^2x_2+2Clx_1x_2-3x_1^2x_2-2Clx_2^2-9x_1x_2^2-23x_2^3)}{15m_Sl}$$

$$H_{77}=\frac{8\pi l(x_1+x_2)}{15M_S}+\frac{8\pi(x_1+x_2)(C^2l^2+2Clx_1+7x_1^2-2Clx_2-4x_1x_2+7x_2^2)}{15m_Sl}.$$

The grain boundary element viscosity matrix is a 4×4 matrix,

$$H^e=\frac{\pi l}{6m_B}\times\begin{bmatrix} S^2(3x_1+x_2) & -SC(3x_1+x_2) & S^2(x_1+x_2) & -SC(x_1+x_2)\\ -SC(3x_1+x_2) & C^2(3x_1+x_2) & -SC(x_1+x_2) & C^2(x_1+x_2)\\ S^2(x_1+x_2) & -SC(x_1+x_2) & S^2(x_1+3x_2) & -SC(x_1+3x_2)\\ -SC(x_1+x_2) & C^2(x_1+x_2) & -SC(x_1+3x_2) & C^2(x_1+3x_2)\end{bmatrix}.$$

References

Brakke, K., 1992. The surface evolver. Experimental Mathematics 1, 141–165; the program is accessible on line http://www.susqu.edu/facstaff/b/brakke/evolver/default.htm.

Brook, R.J., 1969. Pore–grain boundary interactions and grain growth. J. Amer. Ceramic Soc. 52, 56–57.

Carter, W.C., Taylor, J.E., Cahn J.W., 1997. Variational methods for microstructural-evolution theories. JOM-J. Min. Met. Mat. S. 49 (12), 30–36.

Cannon, R.M., Carter, W.C., 1989. Interplay of sintering microstructures, driving forces, and mass transport mechanisms. J. Amer. Ceramic Soc. 72, 1550–1555.

Coble, R.L., 1960. Sintering crystalline solids. I. Intermediate and final state diffusion models. Journal of Applied Physics 32, 787–792.

Coleman, B.D., Falk, R.S., Moakher, M., 1995. Stability of cylindrical bodies in the theory of surface diffusion. Physica D 89, 123–135.

Coleman, B.D., Falk, R.S., Moakher, M., 1996. Space-time finite element methods for surface diffusion with applications to the theory of the stability of cylinders. SIAM J. Sci. Comput. 17, 1434–1448.

Herring, C., 1951. Surface tension as a motivation for sintering. In: Kingston, W.E. (Ed.), The Physics of Powder Metallurgy. McGraw-Hill, New York, pp. 143–179.

Hsueh, C.H., Evans, A.G., 1983. Microstructure evolution during sintering: the role of evaporation/condensation. Acta Metall. 31, 189–198.

Hsueh, C.H., Evans, A.G., Coble, R.L., 1982. Microstructure development during final/intermediate stage sintering-pore/grain boundary separation. Acta Metall. 30, 1269–1279.

Mullins, W.W., 1957. Theory of thermal grooving. J. Appl. Phys. 28, 333–339.

Nichols, F.A., Mullins, W.W., 1976. On the spheroidization of rod shaped particles of finite length. J. Mater. Sci. 11, 1077–1082.

Parhami, F., McMeeking, R.M., Cocks, A.C.F., Suo, Z., 1998. A model for the sintering and coarsening of rows of spherical particles. Mechanics of Materials, in press.

Pharr, G.M., Nix, W.D., 1979. A numerical study of cavity growth controlled by surface diffusion. Acta Metall. 27, 1615–1631.

Rödel, J., Glaeser, A., 1990. Pore drag and pore–boundary separation in alumina. J. Amer. Ceramic Soc., 73, 3302–3312.

Shewmon, P.G., 1964. Movement of small inclusions in solids by a temperature gradient. Trans. Met. Soc. AIME 230, 1134–1137.

Srolovitz, D.J., Safran, S.A., 1986. Capillary instabilities in thin films. J. Appl. Phys. 60, 247–260.

Struik, D.J., 1988. Lectures on Classical Differential Geometry. Dover Publications, New York.

Suo, Z., 1997. Motions of microscopic surfaces in materials. Advances in Applied Mechanics 33, 194–294.

Sun, B., Suo, Z., 1997a. A finite element method for simulating interface motion—II. Large shape change due to surface diffusion. Acta Materialia 45, 4953–4962.

Sun, B., Suo, Z., Yang, W., 1997b. A finite element method for simulating interface motion—I. Migration of phase and grain boundaries. Acta Materialia 45, 1907–1915.